Check for updates

Redox-responsive mesoporous silica nanoparticles based on fluorescence resonance energy transfer for anti-cancer drug targeting and real-time monitoring

Mingxing Liu[1,2,3,a] (iD)**, Jian Liu**[1,2,3]**, Yu Wang**[1,2,3]**, Wanxia Wang**[1,2,3]**, Hongda Zhu**[1,2,3]**,
Huiling Guo**[1,2,3]**, Hongmei Sun**[1,2,3]

[1] *Key Laboratory of Fermentation Engineering (Ministry of Education), Wuhan, China*
[2] *National "111" Center for Cellular Regulation and Molecular Pharmaceutics, Wuhan, China*
[3] *Hubei Key Laboratory of Industrial Microbiology, Hubei University of Technology, Wuhan 430068, China*
[a] Address all correspondence to this author. e-mail: lmxing@hbut.edu.cn

Redox-responsive colloidal mesoporous silica nanoparticles (CMS) drug delivery systems based on fluorescence resonance energy transfer (FRET) was successfully designed for targeting and real-time monitoring in potential cancer therapy. FRET-CMS indicated the typical type IV isotherm with uniform distribution and wormhole arrangement of mesopores. In vitro release studies indicate the redox-sensitive drug release behaviors. Furthermore, the release of entrapped drugs in real time is monitored by the changed FRET signals of FRET-CMS, which is effectively controlled due to the eliminating FRET with the dissociation of FRET donor–acceptor pair. Fluorescent images of cellular uptake and cell viability test revealed that FRET-CMS enhanced significantly 6-MP accumulation in Hela cells with CD44 receptor over-expressed compared to MCF-7 cells due to the existence of hyaluronic acid and subsequently induced selective cytotoxicity to Hela cells. The obtained results illustrate that FRET-CMS may be a promising nanocarrier for drug delivery systems in cancer therapy.

Introduction

In recent years, the ideal stimuli-responsive drug delivery systems (DDSs) are still in great challenges to have the following characteristics: (i) recognize and target tumor cell in high selective manner [1, 2]; (ii) modulate drug release profiles with spatial, temporal, and dosage control [2]; and (iii) monitor drug release in real time [3, 4]. In this regard, mesoporous silica nanoparticles (MSNs) have excellent potential as DDSs due to their high surface area and pore volume, tunable pore size, biocompatibility, and ease of surface functionalization [5, 6] for diverse biomedical applications including diagnostics [7, 8], biosensing [9, 10], biocatalysis [11, 12], bone repair and scaffold engineering [13, 14], and especially drug delivery [5, 15]. The ordered pore network of MSNs allows for entrapping drugs by simple diffusion. Importantly, the pore entrances could be blocked by grafting either bulky molecular groups or nanoparticles on the external surface of MSNs loaded with a particular cargo [16, 17], which were constructed for efficient sealing of the

interior mesoporous environment and triggering the release of the entrapped drug in response to external or internal stimuli including temperature [18, 19], magnetic field [20], light [21, 22], pH [23], redox potential [24], and biomolecule [25, 26].

The development of redox-responsive carrier for intracellular delivery of drug has attracted substantial attention in recent years. The disulfide bond as a redox-responsive bond can be cleaved under a high concentration of glutathione (GSH) with its advantages on the relative stability in extracellular fluids and plasma, and easy rupture in intracellular fluid, since the concentration of GSH in tumor cells (1–10 mM) is nearly 103-fold higher than that of GSH in the plasma environment (2–20 μM) [1, 2]. So drug can be released from nanomaterials functionalized with a nanovalve containing a disulfide bond in specific times in tumour cell.

Fluorescence imaging is one of the most sensitive techniques among all current real-time monitoring strategies. The fluorescence resonance energy transfer (FRET) is a very ideal method to realize the goal [3]. FRET would work on condition

that a fluorescent molecule (donor molecule) has its fluorescence spectrum overlapped with the excitation spectrum of another fluorescent molecule (acceptor molecule), during which the excitation of the donor fluorescent molecule could induce the fluorescence of the acceptor molecule and the fluorescence intensity of the donor fluorescent molecule itself becomes weakened [27, 28]. Furthermore, the degree of FRET is closely related to the spatial distance between the donor and acceptor molecules about 7–10 nm. FRET could be very sensitive to distances (typically less than 10 nm) and significantly attenuated as the donor–acceptor dissociation leads to longer distances, making this unique feature of FRET an ideal tool for monitoring drug release in real time [29, 30]. By engineering such a FRET-active donor–acceptor structure containing the integration of coumarin and FITC within the pore-unlocking event, the release of the drugs entrapped within the pores of the MSN nanocarrier would be monitored followed by the change in the FRET signal. So the use of FRET donor–acceptor pairs provides a new strategy for monitoring drug release in real time.

Zinc is one of the trace elements essential for the human body and plays an important role in regulating the structure and function of enzymes, the transmission of nerve signal, and the expression of genes [31]. In addition, 8-hydroxyquinoline (8-Hq) and its derivatives have attracted a great deal of attention because of their tendency to form stable complexes with metal cations [32]. There was an overlap between the emission of zinc 8-hydroxyquinolinate complexes (Znq) and the maximum absorption of Rhodamine B (RhB), so Rhodamine B and Znq were designed as FRET donor–acceptor pairs for DDSs in this paper. Hyaluronic acid (HA) has been widely used for DDS due to a specific interaction with CD44 receptors that are overexpressed on various cancer cells [33, 34]. So, the rhodamine B-ethylenediamine-hyaluronic acid (RhB-EA-HA) as a targeting ligand was designed to combine the targeting of materials with the real-time monitoring capabilities in this paper.

Herein, the DDSs of redox-responsive colloidal mesoporous silica nanoparticles based on FRET (FRET-CMS) have been successfully constructed for drug targeting and real-time monitoring. The synthesis route of Znq-CMS and drug-loaded FRET-CMS are shown in Fig. 1a and b, respectively. The properties of particles were successfully characterized. The disulfide bond would be cleaved in the presence of GSH, resulting in the separation of the energy donor (Znq-CMS) from the energy receptor (rhodamine B), followed by the disappearance of FRET and the gradual recovery of green fluorescence of the energy donor (Fig. 1c). Meanwhile, the BSA adsorbance, cellular uptake, and cell viability of FRET-CMS were investigated in this paper.

Results and discussion

Preparation and characterization of particles

The physicochemical feature of particles was investigated. SEM image of CMS-SH and FRET-CMS had an approximately spherical morphology with relatively uniform particle size and an average particle diameter of about 85 nm (Fig. 2a and b). TEM image of CMS-SH and FRET-CMS displayed a spherical morphology and uniform distribution with a wormhole arrangement of mesopores (Fig. 2c and d). However, compared with the obvious mesoporous structure of CMS-SH, the mesoporous structure of FRET-CMS became almost invisible due to the encapsulation of RhB-EA-HA on the surface of nanoparticles. The hydrodynamic diameter was increased from 113.2 nm for CMS-SH to 434.1 nm for FRET-CMS, even though the average size of nanoparticles measured by DLS was larger than that of TEM and SEM due to the hydration layer measured in aqueous conditions (Fig. 2g).

The surface area and average pore size of CMS-SH and FRET-CMS were substantiated by N_2 adsorption–desorption isotherms. The typical IV isotherm type of CMS-SH and FRET-CMS remained still after encapsulated with Rhb-EA-HA (Fig. 2e). From Table 1, the S_{BET}, V_t, and W_{BJH} of FRET-CMS were obviously decreased compared to that of CMS-SH, especially the SBET gradually decreased from 1225 m^2/g of CMS-SH to 599 m^2/g of FRET-CMS.

FT-IR spectra of CMS, CMS-SH, Znq-CMS, and Znq-CMS-COOH are shown in Fig. 2f. Compared with the infrared spectrum of CMS-SH, the characteristic peak of mercapto group disappeared at 2561 cm^{-1} after doping Znq by in-situ method and the appearance of peaks at 1500, 1465, 1384, and 1322 cm^{-1} were the vibrational peaks of the pyridyl and phenyl groups of Znq. The peak appeared at 1633 cm^{-1} was attributed to the stretching vibration of carbonyl.

The charge changes of nanomaterials were investigated (Fig. 2h). The zeta potential of CMS-SH had significant change from − 27.8 mV, to − 16.5 mV, to − 43.4 mV, to + 30.6 mV, successively, due to the introduction of Zn^{2+} and 8-hydroxyquinoline on the surface of CMS-SH, modified by –COOH [35]. After coating with Rhb-EA-HA, the zeta potential converted to − 36.8 mV due to the shielding effect of polymer, confirming the successful modification of Rhb-EA-HA.

RhB-EA-HA as FRET receptor was successfully synthesized with hyaluronic acid and rhodamine B by the amide reaction (Fig. 3a). The chemical structure of RhB-EA-HA was characterized by FT-IR, UV, and ^1H NMR. ^1H NMR of RhB and RhB-EA-HA are shown in Fig. 3b and c. The peaks at $\delta 8.19$, $\delta 7.77$, $\delta 7.40$, and $\delta 7.00$ were attributed to the chemical shifts of hydrogen protons on the aromatic ring in RhB and RhB-EA-HA. The peaks at $\delta 2.0$ and $\delta 5.06$ were ascribed to the hydrogen proton of methyl group on hyaluronic acid and attached to the hydroxyl group on hyaluronic acid, respectively. Moreover, the peaks at
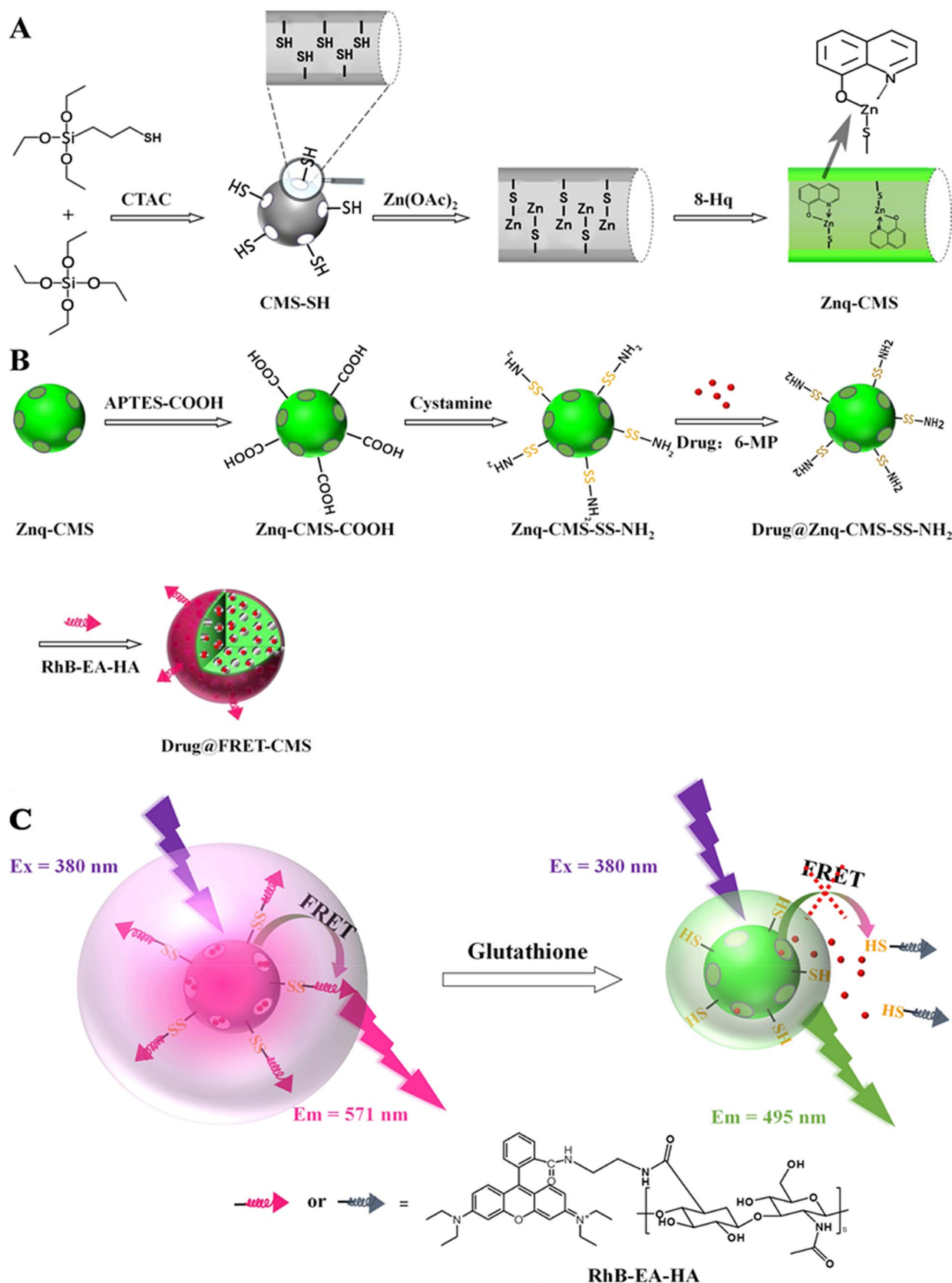
Figure 1: The synthesis route of particles and schematic representation of FRET principle. (a) The synthesis route of Znq-CMS. (b) The synthesis route of FRET-CMS. (c) Schematic representation of FRET principle.
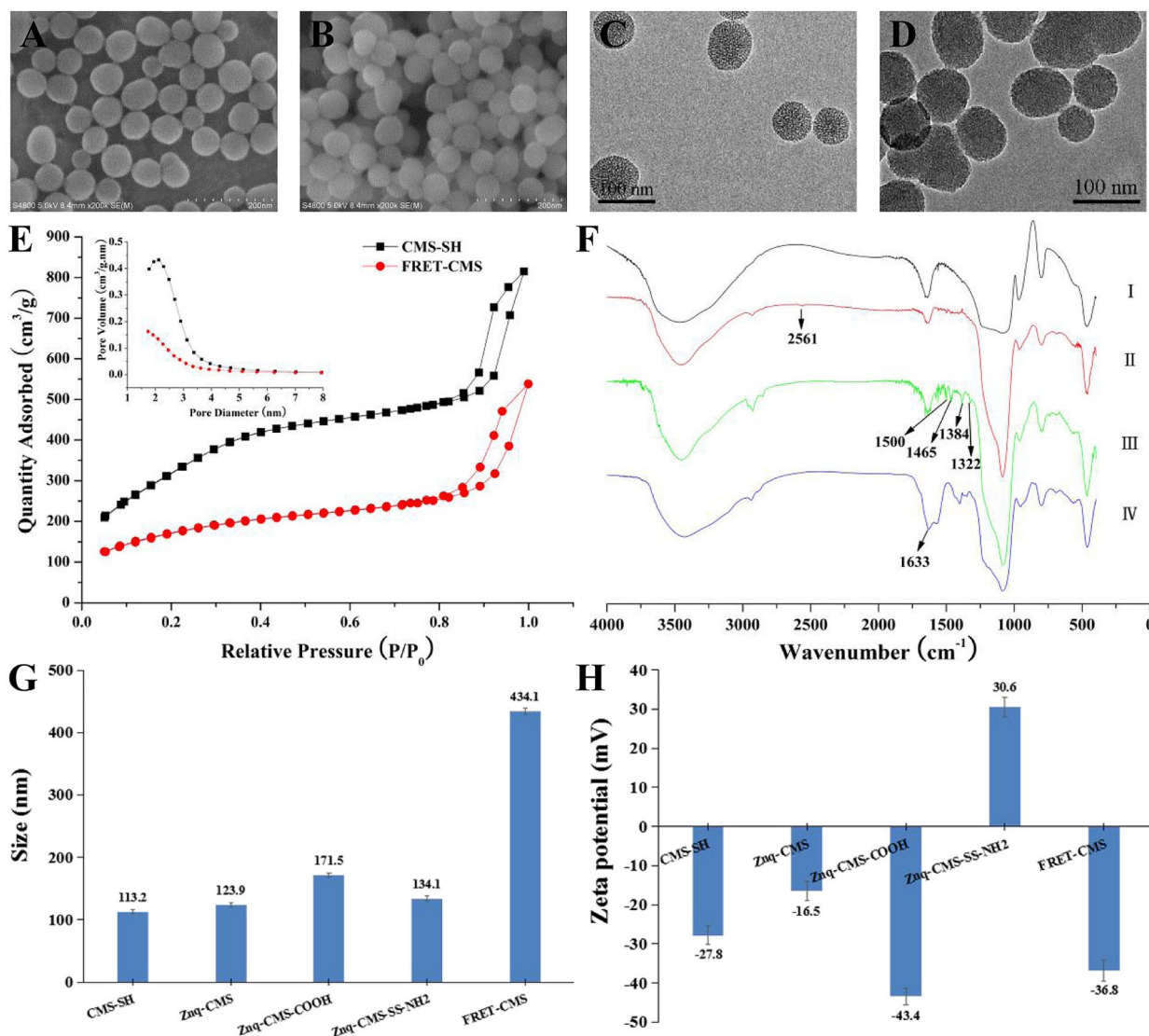
Figure 2: Characterization of particles. (a) and (b) are SEM images of CMS-SH and FRET-CMS, respectively. (c) and (d) are TEM images of CMS-SH and FRET-CMS, respectively. (e) N₂ adsorption–desorption isotherms and pore size distributions of CMS-SH and FRET-CMS. (f) FT-IR spectra of CMS (I), CMS-SH (II), Znq-CMS (III), and Znq-CMS-COOH (IV). (g) and (h) are DLS size and zeta potential of CMS-SH, Znq-CMS, Znq-CMS-COOH, Znq-CMS-SS-NH2, FRET-CMS, respectively.

TABLE 1: Nitrogen adsorption–desorption analysis of CMS-SH and FRET-CMS.

Materials	S_{BET} (m²/g)[a]	V_t (cm³/g)[b]	W_{BJH} (nm)[c]
CMS-SH	1225 ± 11.8	1.26 ± 0.03	2.1 ± 0.04
FRET-CMS	599 ± 6.1	0.83 ± 0.01	1.46 ± 0.03

Data were expressed values as mean ± SD ($n = 3$).

[a]S_{BET} is the B–E–T surface area calculated at a relative pressure of P/P0 from 0.064 to 0.199.

[b]V_t is the total pore volume measured at a relative pressure of 0.974.

[c]WBJH is the pore size distribution calculated by the B–J–H method on the desorption branches of the nitrogen isotherms.

δ1.26 and δ1.12 were attributed to the two methylene proton of ethylenediamine coupling RhB and hyaluronic acid. FT-IR of RhB (I), RhB-EA (II), and RhB-EA-HA (III) is shown in Fig. 3d, the peaks at 2969 cm⁻¹ and 2929 cm⁻¹ can be attributed to the asymmetric stretching vibration of methyl and methylene groups in RhB, respectively. The absorption peak at 1500 cm⁻¹ was assigned to the skeleton stretching vibration of benzene ring. The peak of RhB retained and a new peak at 1633 cm⁻¹ appeared in the infrared spectra of RhB-EA and RhB-EA-HA were attributed to the carbonyl stretching vibration of the amide bond, indicating the formation of RhB-EA and RhB-EA-HA by amide reaction with ethylenediamine. The UV analysis of HA, RhB, and RhB-EA-HA was applied to further demonstrate the
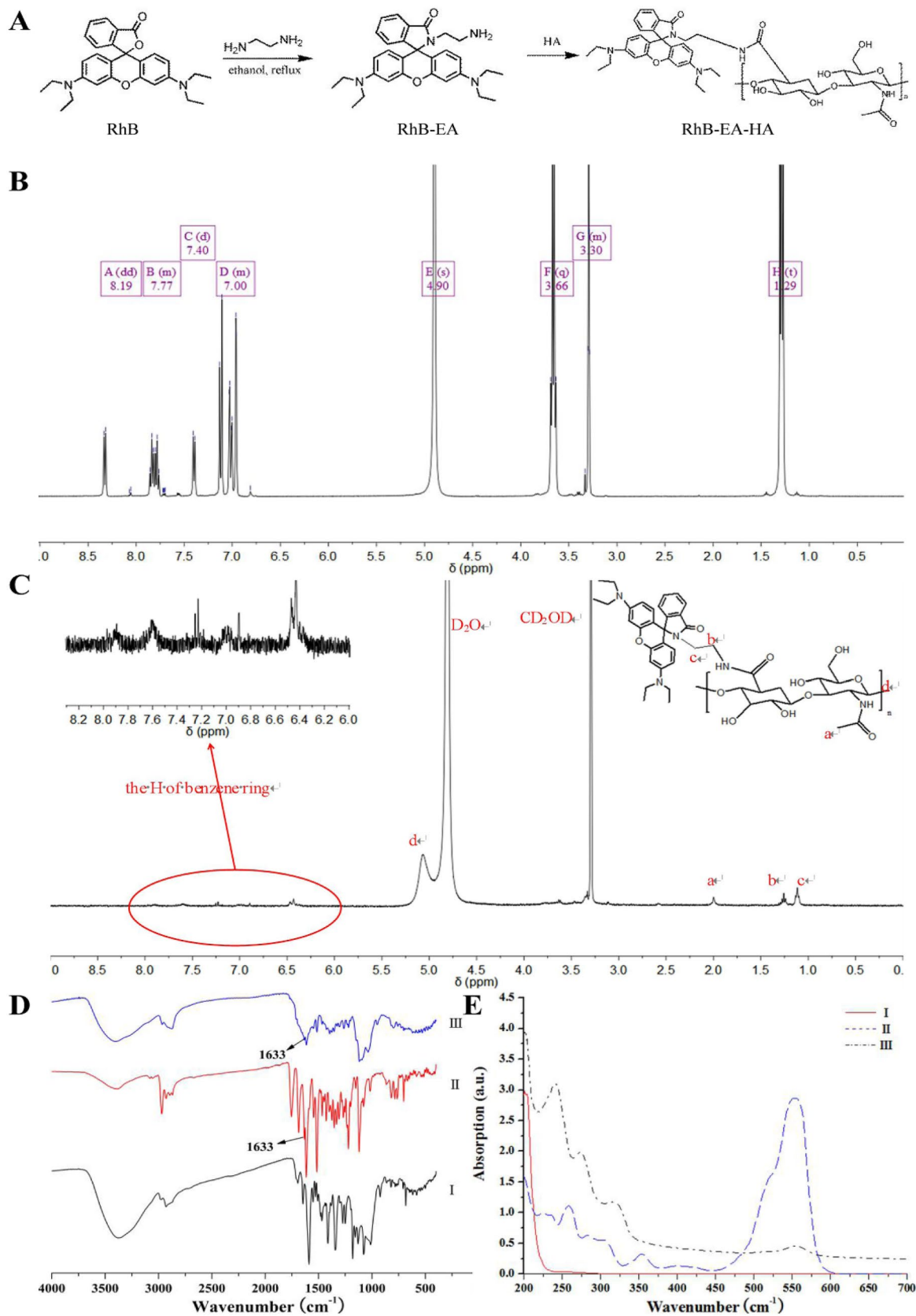
Figure 3: The synthesis route and characterization of RhB-EA-HA. (a) The synthesis route of RhB-EA-HA. (b) 1H NMR spectra of RhB in CD3OH. (c) 1H NMR spectra of RhB-EA-HA in D2O:CD3OH = 1:1. (d) FT-IR spectra of RhB (I), RhB-EA (II), and RhB-EA-HA (III). (e) UV spectra of HA (I), RhB (II), and RhB-EA-HA (III).

successful synthesis of RhB-EA-HA. The strong absorption peak at 554 nm attributed to the presence of aromatic fused heterocycles was shown in the RhB-EA (II) and RhB-EA-HA (III) and there was no UV absorption in HA (I) (Fig. 3e).

Fluorescence intensity changes of FRET-CMS at 495 nm (green) and 571 nm (red) were investigated in the presence of different concentrations of GSH in pH 7.4 PBS (Fig. 4f). With the increase concentration of GSH, the fluorescence intensity at 571 nm gradually decreased and the fluorescence intensity at 495 nm gradually increased. Only single peak at 495 nm appeared in the presence of 10 mM GSH. The phenomenon indicated that the cleavage of disulfide bond in GSH results in the dissociation of donor–acceptor, further leading to the FRET closed and the green fluorescence of nanocarrier gradually recovered. So, GSH could control the switch of FRET, which provided a potential application for real-time monitoring of GSH-induced release of nonfluorescent drugs.

Fluorescence properties of nanoparticles

The fluorescence properties of nanoparticles were very important and were also investigated by the fluorescence spectrophotometer in this paper (Fig. 4). The dispersion of Znq-CMS had a strong green fluorescence under UV light irradiation, with a fluorescence emission wavelength of 510 nm at an excitation wavelength of 380 nm and a slit of 10 nm (Fig. 4a). The fluorescence emission wavelength and intensity did not significantly change after 1 and 2 months in ethanol solution, indicating that the fluorescence properties of Znq-CMS were relatively stable in a certain period of time. In addition, the effects of different pH on the fluorescence properties of Znq-CMS were also investigated (Fig. 4b and g). The fluorescence intensity of Znq-CMS remained relatively stable with abroad pH range from 5 to 9 in PBS. However, the fluorescence intensity was greatly diminished in PBS with pH < 5 and almost completely vanished when the pH dropped to 3, indicating the excellent fluorescent stability of Znq-CMS. It was reported [36] that pH of endosomes or lysosomes in the tumor micro-environment reaches a minimum of about 5.0 [37]. Therefore, the fluorescence intensity of Znq-CMS in physiological conditions and tumor microenvironment would not be greatly affected.

The fluorescence spectra of nanomaterials obtained after modification were determined to confirm changes of the fluorescence spectra of mesoporous silica nanoparticles. Although
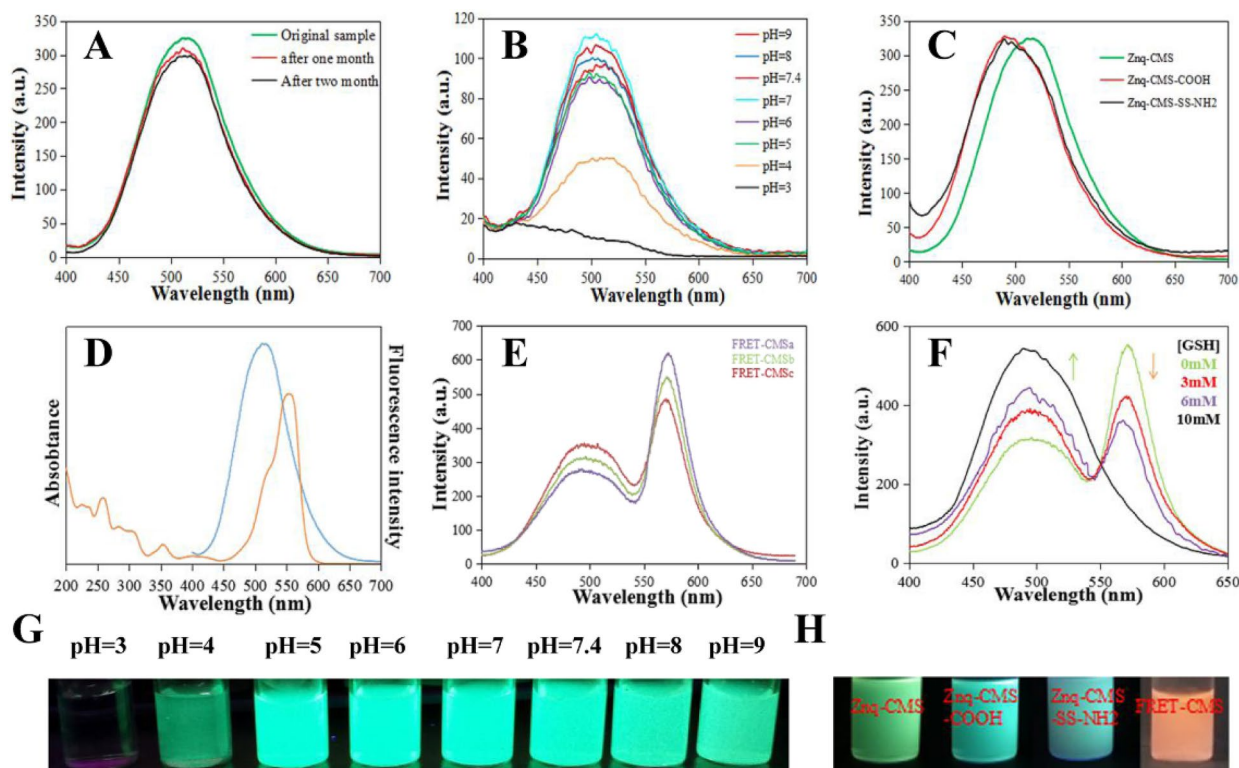

Figure 4: The fluorescence spectra and characterization of particles. (a) The fluorescence spectra of Znq-CMS at different times. (b and g) The fluorescence spectra and characterization of Znq-CMS in different pH buffers, respectively. (c) The fluorescence spectra of Znq-CMS, Znq-CMS-COOH, and Znq-CMS-SS-NH2. (d) Spectrum overlaps between UV of RhB and the emission of FRET-CMS. (e and h) The fluorescence signal changes by FRET-CMS excited at 380 nm and the corresponding fluorescent photos of the samples under 365 nm UV light, respectively. (f) The fluorescence intensity changes of FRET-CMS at 495 nm and 571 nm in different concentrations of GSH at pH 7.4.

the maximum fluorescence emission peak of Znq-CMS was shifted from 510 to 495 nm after two steps of modification, the fluorescence spectra still overlap with the absorption spectrum of FRET receptor RhB without affecting the construction of FRET-CMS (Fig. 4c). In addition, the fluorescence intensity of each step of modification nanoparticles was gradually weakened consistent with the results of the fluorescent photos (Fig. 4h). Znq in Znq-CMS can be excited by absorbing light with a wavelength of 380 nm, resulting in the emission of light in the range of 450–550 nm (Fig. 4d). When the disulfide bond was intact, the Znq in Znq-CMS excited at 380 nm would act as a FRET donor for the RhB-EA-HA with absorbance maximally at 554 nm. The dual emission peaks at 495 nm and 571 nm displayed in the fluorescence spectra of FRET-CMS upon excitation at 380 nm were attributed to the fluorescence of Znq-CMS and RhB, respectively, indicating that the induce of donor–acceptor FRET system lead to the production of fluorescence of the energy receptor rhodamine B (Fig. 4e). The different FRET-CMS obtained with the increasing concentration of RhB-EA-HA

lead to an increase in the fluorescence of RhB with negligible quenching of fluorescence of quinoline zinc, indicating that the fluorescence resonance energy transfer could be promoted by increasing the amount of energy receptor.

Drug release study in vitro

The highest drug loading efficiency and encapsulation efficiency of 6-MP@FRET-CMS were up to 6.3% and 37.8%, respectively.

The drug release of 6-MP@FRET-CMS was investigated in different pH of PBS and the different concentrations of GSH (Fig. 5). With the increasing concentration of GSH, the amount of 6-MP released was significantly increased (Fig. 5a). The cumulative release of 6-MP reached 5.2%, 7.5%, 28.2%, and 81.3% within 24 h when concentrations of GSH were 0 mM, 0.01 mM, 2 mM, and 10 mM, respectively. Meanwhile, almost no premature release was observed in the low concentration of GSH within 24 h, indicating that 6-MP might effectively avoid abrupt release from FRET-CMS due
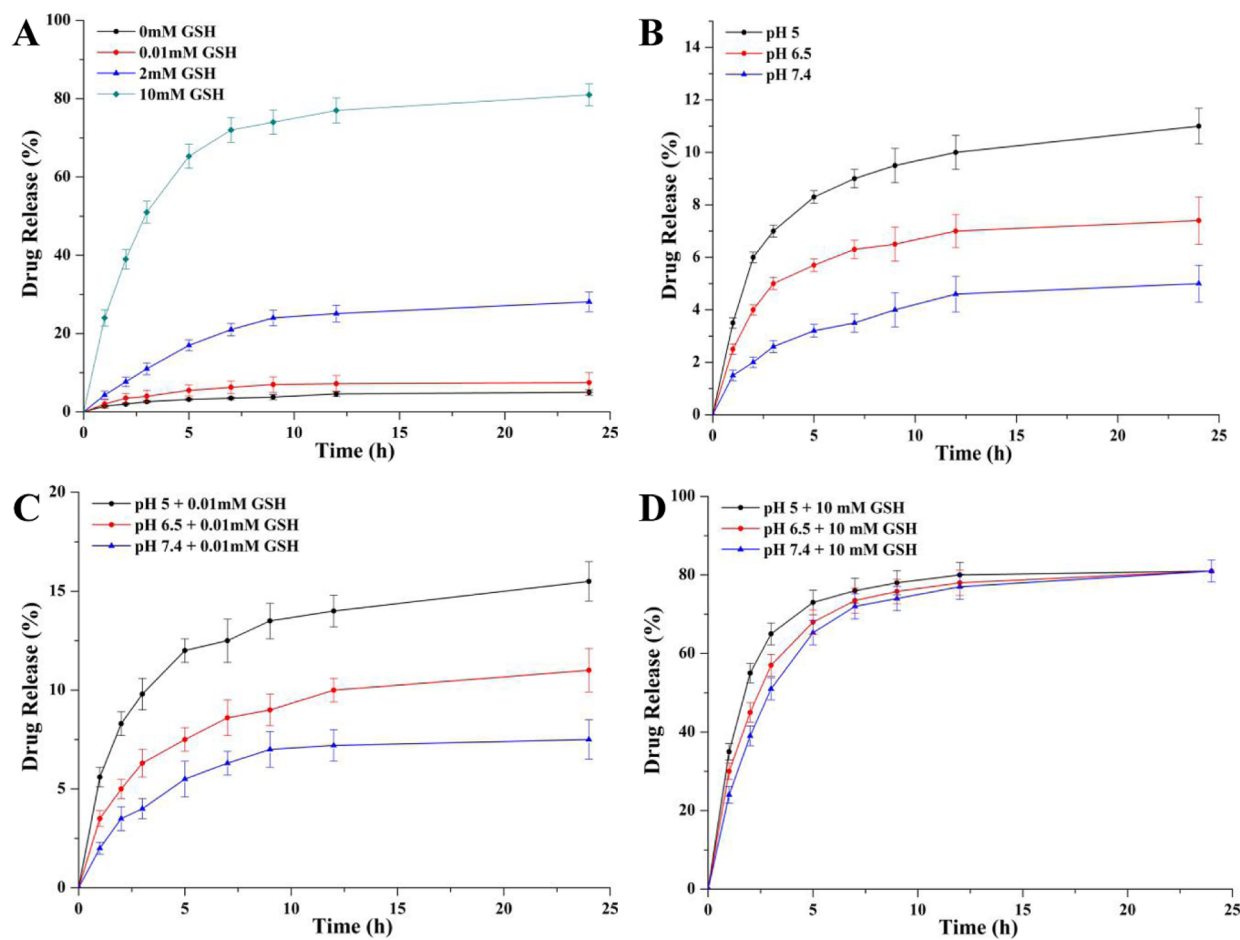

Figure 5: Drug release in vitro profile of 6-MP@FRET-CMS in different release media. (a) Different concentrations of GSH in pH 7.4 PBS. (Values shown mean ± SD; $n = 3$) (b) Different pH of PBS. (Values shown mean ± SD; $n = 3$) (c) Different pH PBS in 0.01 mM GSH. (Values shown mean ± SD; $n = 3$) (d) Different pH PBS in 10 mM GSH. (Values shown mean ± SD; $n = 3$).

to the RhB-EA-HA blocking up the mesopores on the surface of particles. With the concentration of 10 mM GSH, the release of drug reached 39% within the first 2 h due to the cleavage of disulfide bonds. Hence, FRET-CMS as the effective drug carrier had ability to control the drug release by GSH. The amount of 6-MP released was less than 12% in pH 5.0, 6.5, and 7.4 PBS solution within 24 h, However, the release of drugs was promoted slightly with the pH reducing (Fig. 5b). The release behavior was affected by GSH and pH (Fig. 5c and d). The cumulative release reached less than 16% in pH 5.0, 6.5, and 7.4 PBS with 0.01 mM GSH. With further increase in the concentration of GSH to 10 mM (Fig. 5c), the cumulative release reached up to 81% within 24 h and the drug release rate was promoted slightly with the pH reducing (Fig. 5d). Therefore, the grafting of RhB-EA-HA on the surface of CMS-SH via a disulfide linkage could possibly render the carrier with redox-responsive and weak pH-responsive drug delivery capability, which might be beneficial to control the drug release.

BSA adsorption and hemolytic behavior of blank nanoparticles

BSA could be nonspecific adsorbed by mesoporous silica nanoparticles in vitro [38]. So BSA adsorbed to the surface of nanomaterials was measured to investigate the effectiveness of the different modification nanomaterials in our paper. The amounts of BSA adsorbed by CMS-SH, Znq-CMS, Znq-CMS-SS-NH$_2$, and FRET-CMS were 14.5%, 12%, 10%, and 2.5%, respectively (Fig. 6a). The results of BSA adsorption indicated that RhB-EA-HA might affect the adsorption of BSA by changing the steric hindrance of the nanoparticles and the charge ability on the surface of nanomaterials.

The hemolytic images of CMS-SH, Znq-CMS, Znq-CMS-SS-NH$_2$, and FRET-CMS were in the concentration range from 20 to 1500 µg/mL (Fig. 6c). The percentage hemolysis of nanomaterials was related to the concentration over a wide concentration range of 20 to 1500 µg/mL (Fig. 6b). When the concentration of the samples reached 500, 1000, and 1500 µg/mL, the percentage hemolysis of CMS-SH, Znq-CMS, Znq-CMS-SS-NH$_2$, was (3%, 9%, 87%), (2%, 10%, 98%), and (1%, 32%, 64%), respectively. The percentage hemolysis of FRET-CMS as
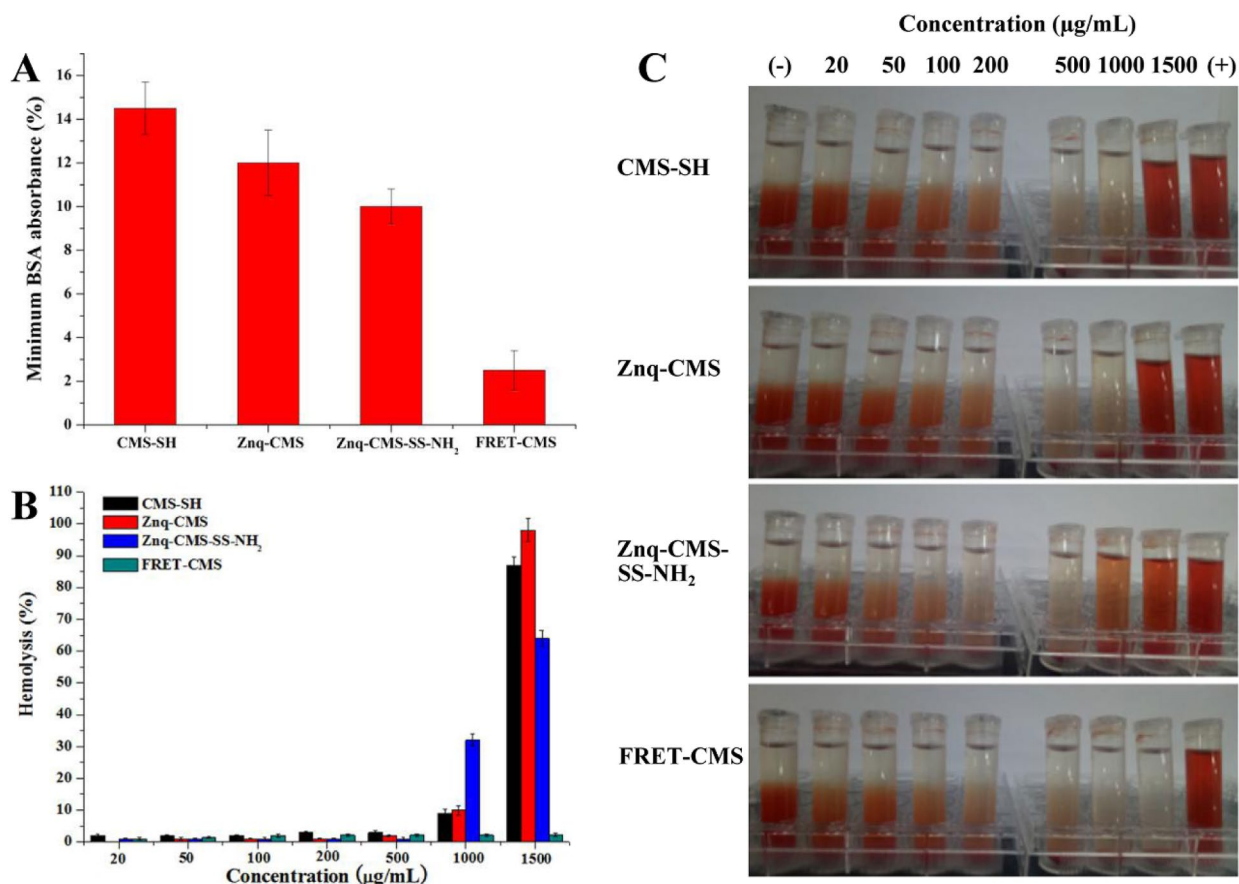

Figure 6: The minimum BSA adsorbance measurements. (*A*) The minimum BSA adsorbance of CMS-SH, Znq-CMS, Znq-CMS-SS-NH$_2$, and FRET-CMS. (Values shown mean ± SD; n = 3) (b) and (c) The hemolysis percentages and hemolytic photographs of CMS-SH, Znq-CMS, Znq-CMS-SS-NH$_2$, and FRET-CMS at different concentrations (µg/mL), respectively.

expected decreased significantly to 2.3% at an extremely high concentration (1500 μg/mL). The hemolytic images show that FRET-CMS presented excellent dispersibility and stability in saline containing rabbit blood cells (RBCs) at high concentrations up to 1500 μg/mL. The percentage hemolysis of nanomaterials was related to the concentration over a wide concentration range of 20 to 1500 μg/mL. The high degree of hemolysis raised serious safety concerns regarding the application of nanomaterials for drug delivery. The explanations for the hemolysis included reactive oxygen species (ROS) induced via the surface of the silica [39, 40], denaturation of membrane proteins by electrostatic inter-actions with silicate [41], and the high affinity of silica for binding with tetra-alkyl ammonium groups that are plentiful in RBC membranes [40]. Therefore, the modification of the RhB-EA-HA on the surface of CMS-SH could significantly improve the biocompatibility of CMS-SH by reducing ROS, the electrostatic interactions, and the affinity between CMS and the tetraalkylammonium groups.

Cytotoxicity assay in vitro

There was no significant difference in cell viability incubation with 6-MP between Hela and MCF-7 cells. The viability of MCF-7 cells after incubation with FRET-CMS for 48 h at the concentrations of 10 and 30 μg/mL was 76.1% and 62.5%, respectively. In contrast, the viability of Hela cells with the same concentration of FRET-CMS reduced to 50.2% and 40.8%, respectively. With the same concentration of FRET-CMS, the viability of MCF-7 cells after incubation for 48 h was more than Hela cells. The results were all consistent with the live/dead staining images, in which the cells with 6-MP and 6-MP@FRET-CMS were stained red (dead cells), only few cells were green (live cells) at high concentration. The significantly different viability between the two cells could be explained by the improved cellular uptake of FRET-CMS with HA receptor-mediated endocytosis [42, 43].

To evaluate the cytotoxicity of 6-MP, Znq-CMS-SS-NH$_2$, FRET-CMS, and 6-MP@FRET-CMS, the HeLa cells and MCF-7 cells were incubated with these samples with various concentrations for 48 h. The cell viabilities were evaluated via live/dead staining and MTT assay. Nearly all of the cells with Znq-CMS-SS-NH$_2$ and FRET-CMS were stained green (live cells) at different concentrations, only few cells were stained red (dead cells) at a high concentration (Fig. 7a and b). Consistent with the live/dead staining of the blank materials, no obvious cytotoxicity could be seen both in HeLa cells (Fig. 7c) and MCF-7 cells (Fig. 7d), and the cell viabilities were all above 87% within the examined concentration range, indicating the good safety of nanoparticles as carriers. 6-MP dose-dependent behavior was shown in Hela and MCF-7 cells treated with free 6-MP and 6-MP@FRET-CMS.

Cellular uptake in vitro

The specific uptake of nanocarriers by cancer cells is particularly critical for the efficient antitumor drug delivery except for the applicable biocompatibility. The cellular uptake of FRET-CMS was systematically investigated with Hela and MCF-7 cells by incubation with Rhb-EA-HA, Znq-CMS-SS-NH$_2$, and FRET-CMS for 1, 2, or 4 h, respectively. Comparing the uptake of RhB-EA-HA by the two kinds of cells, the fluorescence intensity of RhB-EA-HA in Hela cells at 4 h was obviously stronger than that at 1 h and 2 h (Fig. 8a). It was also obvious to observe the red fluorescence in Hela cells at 4 h (Fig. 8e), and there was almost no red fluorescence observed in MCF-7 cells (Fig. 8b and f). Compared with FRET-CMS, there was no obvious difference of the green fluorescence observed in both cells at 4 h (Fig. 8c and d). The fluorescence intensity of RhB-EA-HA in Hela cells indicated that the uptake of RhB-EA-HA by Hela cells was time-dependent. It was also obvious to observe the red fluorescence in Hela cells at 4 h due to the RhB-EA-HA of the surface of FRET-CMS. However, the results of almost no red fluorescence in MCF-7 cells proclaimed the targeting of RhB-EA-HA and FRET-CMS to Hela cells. A small amount of green fluorescence of the material gradually emerged in cells incubated with FRET-CMS due to the cleavage of the disulfide bonds of the material in GSH over-expressed in the cells. Compared with FRET-CMS, no obvious difference of the green fluorescence was observed in both cells at 4 h. These results indicated that the Rhb-EA-HA played a important role in targeting the materials to Hela cells with CD44 receptor over-expressed.

Based on the results of this study, FRET-based redox-responsive mesoporous silica nanoparticles as a promising nanocarrier would have great potential for drug targeting delivery. Further studies are warranted to evaluate the in vivo process of 6-MP@FRET-CMS by animal experiments.

Conclusions

In summary, we have successfully prepared a redox-responsive mesoporous silica nanoparticles drug delivery systems based on fluorescence resonance energy transfer (FRET-CMS) for drug targeting and real-time monitoring. The RhB and Znq of FRET-CMS could be integrated as FRET donor–acceptor pair to monitor the release of 6-MP from the pores in real time. In vitro release studies indicated the redox-sensitive drug release behaviors. Furthermore, the changed FRET signals of FRET-CMS with the dissociation of FRET donor–acceptor pair were controlled by the cleavage of disulfide bond in glutathione (GSH), which rendered the nanomaterials with the ability to monitor the release of
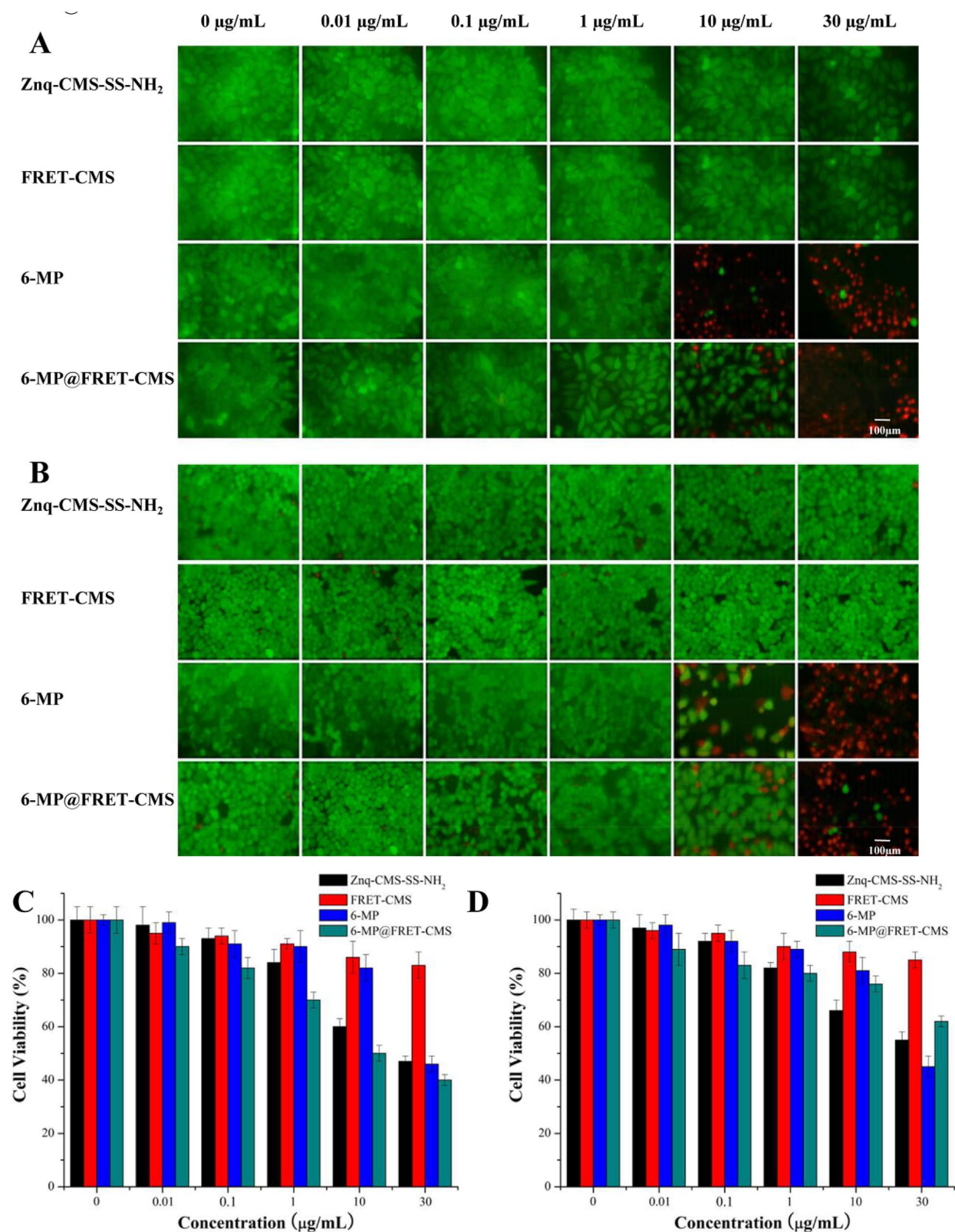
Figure 7: Cytotoxicity assay in vitro. (a) and (b) Fluorescence images of Hela cells and MCF-7 cells for Znq-CMS-SS-NH$_2$, FRET-CMS, free 6-MP, and 6-MP@FRET-CMS with different concentrations for 48 h, respectively. (*Note* The live cells were stained green, and the red indicates the dead cells.) (c) and (d) Cell viability of Hela cells and MCF-7 cells after incubated with the above samples with different concentrations for 48 h, respectively. (Values shown mean ± SD; $n = 3$).
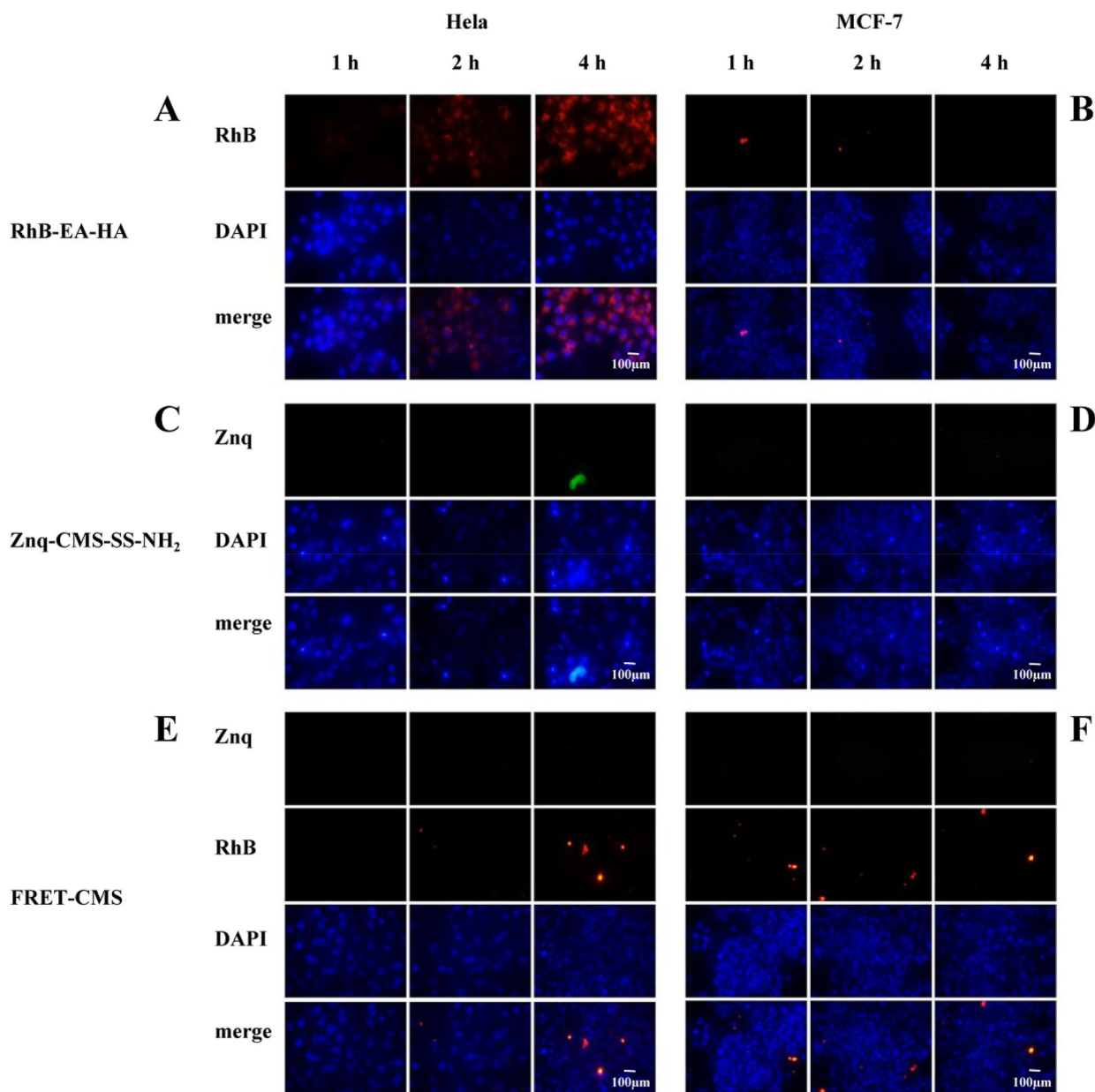
Figure 8: Cellular uptake in vitro. (a) and (b) Fluorescence microscopy images of Hela and MCF-7 cells incubated with RhB-EA-HA for different times (1 h, 2 h, and 4 h), respectively. (c) and (d) Fluorescence microscopy images of Hela and MCF-7 cells incubated with Znq-CMS-SS-NH$_2$ for different times (1 h, 2 h, and 4 h), respectively. (e) and (f) Fluorescence microscopy images of Hela and MCF-7 cells incubated with FRET-CMS for different times (1 h, 2 h, and 4 h), respectively. (*Note* RhB-EA-HA and FRET-CMS containing RhB were visualized with red fluorescence, the nuclei were stained blue with DAPI, and the images below indicated the merged fluorescence.).

entrapped drugs in real time. The results of BSA adsorption and hemolytic behavior of blank nanoparticles revealed that the RhB-EA-HA as a targeting ligand modified on the surface of Znq-CMS could improve the stability and biocompatibility of Znq-CMS. The cellular uptake performance of FRET-CMS showed a higher cellular uptake performance via CD44 receptor-mediated endocytosis in Hela cells with CD44 receptor over-expressed than in MCF-7 cells. 6-MP-loaded FRET-CMS exhibited greater cytotoxicity against Hela cells than MCF-7 cells due to the enhanced cell uptake behavior of FRET-CMS. The cellular targeting assay demonstrated that FRET-CMS could specifically target tumor cells, suggesting that the nanomaterials might minimize the potential damage to the normal cells. Therefore, the excellent properties of FRET-CMS might make it a excellent redox-responsive nanocarrier for targeting drug delivery and monitoring drug release in real time.

Materials and methods

Materials

Tetraethoxysilane (TEOS), triethanolamine (TEA), cetyltrimethylammonium chloride (CTAC), 3-(Triethoxysilyl) propan-1-amine (APTES), bovine serum albumin (BSA), and rhodamine B were obtained from Aladdin Chemistry, Co., Ltd. 3-Mercapto-propyltriethoxysilane (MPTES, 95%), 8-Hydroxyquinoline (Hq), N-hydroxysuccinimide (NHS, > 98%), and Cystamine dihydrochloride were all purchased from Shanghai Macklin Biochemical Technology Co., Ltd. N-(3-dimethylaminopropyl)-N-ethylcarbodiimide hydrochloride (EDC, 99%) and 6-mercaptopurine (6-MP) were purchased from J&K Scientific. Zinc acetate dihydrate, ethylenediamine, Dichloromethane, dimethyl sulfoxide (DMSO), and hydrochloric acid (HCl, 37%) were supplied by Sinopharm Chemical Reagent Co., Ltd. Sodium hyaluronate (HA) (Mw 10,000 kDa) was obtained from Fusheng Industrial Shanghai Co., Ltd. Fluorescein diacetate (FDA) and glutathione (GSH) were obtained from Sigma-Aldrich. 3-(4,5-Dimethylthiazol-2-yl)-2,5-diphenyl tetrazolium bromide (MTT) was supplied by Guangzhou Saiguo Biotech Co., Ltd. Cell culture Dulbecco's modified Eagle's medium (DMEM), trypsin, phosphate-buffered saline (PBS), penicillin–streptomycin, fetal bovine serum (FBS), Paraformaldehyde, and 4,6-diamidino-2-phenylindole (DAPI) were obtained from Bestbio. Propidium Iodide (PI) was obtained from Beijing Solarbio Science & Technology Co., Ltd. Rabbit anticoagulant whole blood was supplied by Beijing Borsi Technology Co., Ltd. All other chemicals were of analytical grade and used without further purification.

Synthesis of CMS-SH

CMS-SH was prepared by the co-condensation method [44]. A mixture of 64 mL of water, 10.5 mL of ethanol, and 10.4 mL of 25 wt% CTAC were stirred for 10 min at room temperature, followed by an addition of 4.125 mL of triethanolamine and the mixture was stirred for another 15 min as a stock solution. The 40 mL of the stock solution was heated to 60 ℃ in the oil bath, followed by a dropwise addition of a mixture of 2.9 mL TEOS and 0.325 mL MPTES within 2–3 min and stirred for 2 h at 60 ℃ under nitrogen atmosphere. The product was collected by centrifugation at 10,000 rpm for 30 min and washed twice with ethanol. The resulting product was refluxed twice in the solution of 10 mL of hydrochloric acid and 90 mL of ethanol at 60° C for 2 h, and then the surfactant-removed CMS-SH was centrifuged, washed with distilled water and ethanol several times, and redispersed in ethanol solution (5 mg/mL) for the following use.

Synthesis of Znq-CMS

20 mL of CMS-SH was centrifuged and washed with ultrapure water, and then centrifuged and redispersed in 9.5 mL of 0.05 mol/L Zn(Ac)$_2$ solution. The mixture was stirred at room temperature for 12 h. The nanoparticles were collected by centrifugation at 8000 rpm for 10 min and washed with ethanol three times, and then redispersed in water. 9.7 mg of 8-hydroxyquinoline (8-Hq) dissolved in 25 mL of ethanol was added dropwise to 20 mL of 5 mg/mL of the above solution at room temperature under stirring for 48 h. The resulting solids of fluorescent mesoporous silica nanoparticles (Znq-CMS) were centrifuged at 10,000 r/min for 20 min and washed with ethanol until the supernatant was colorless, and finally dispersed in ethanol.

Synthesis of Znq-CMS-SS-NH$_2$

20 mL of Znq-CMS ethanol solution (5 mg/mL) was added 10 μL of ammonia water, and followed by the addition of 104 mg of APTES-COOH dissolved in 2 mL of ethanol which was synthesized by APTES and maleic anhydride stirring at 0 ℃ for 15 min. The mixture solution was stirred at room temperature for 12 h. The Znq-CMS-COOH was obtained by centrifuging at 10,000 r/min for 15 min and washing with ethanol three times. The Znq-CMS-COOH was redispersed in 20 mL of water and then activated by 120 mg of EDC·HCl and 80 mg of NHS at room temperature for 1 h, followed by the addition of 0.5 g cystamine dihydrochloride dissolved in 5 mL water. The mixture was stirred at room temperature for 12 h in the dark. The amino-terminated fluorescent mesoporous silica nanoparticles containing disulfide bonds (Znq-CMS-SS-NH$_2$) were obtained by centrifuging at 10,000 r/min for 15 min and washing with distilled water three times, and then redispersing in water.

Preparation of RhB-EA-HA

2.40 g of Rhodamine B was dissolved in 60 mL of ethanol, followed by adding dropwise 0.43 mL of Ethylenediamine under vigorous stirring at room temperature. The reaction solution was refluxed for 12 h. After the mixture solution cooled to room temperature, the solvent was distilled off under reduced pressure. In order to remove the unreacted ethylenediamine, 1 M HCl (about 100 mL) was added to the residue, followed by the addition of 1 M NaOH (about 140 mL) under stirring until the pH of the solution reached 9–10. The resulting solution was extracted three times with dichloromethane (3 × 100 mL). The organic phase was washed with 50 mL of water and dried with Na$_2$SO$_4$. The RhB-EA was obtained by evaporating the solvent and dried under vacuum at 40 ℃ for 12 h. 100 mg of HA was dissolved in 50 mL of water, and activated by adding 150 mg of EDC·HCl and 100 mg of NHS at room temperature reaction for 1 h. Then, 10.5 mg of RhB-EA dissolved in water was added dropwise to the solution, followed by stirring for 24 h at room temperature in the dark. The product was dialyzed against

Ultra-pure water for two days (6 times water change) with dialysis bag (Mw cutoff 14 kDa) to remove unreacted free HA, EDC, and NHS, and finally freeze-dried for the following use.

Synthesis of Znq-CMS-SS-RhB-EA-HA (FRET-CMS)

1 mg/mL of RhB-EA-HA aqueous solution was obtained by dissolving 30 mg of RhB-EA-HA in 30 mL of water and activated by 90 mg EDC·HCl and 60 mg of NHS at room temperature for 1 h, followed by an addition of 20 mL of the Znq-CMS-SS-NH$_2$ suspension (5 mg/mL) and the solution was allowed to stir for 24 h at room temperature in the dark. The FRET-CMS particles were then obtained after centrifugation at 10,000 rpm for 15 min and washed with deionized water for several times, and finally dispersed in water.

Preparation method of samples for evaluating FRET switch

5 mg of FRET-CMS was dispersed in 20 mL of PBS buffer (pH 7.4) in the presence of different concentrations of glutathione (0 mM, 3 mM, 6 mM, 10 mM) and stirred for 15 min at room temperature, respectively. The nanoparticles were then centrifuged, washed three times with pH 7.4 PBS, redispersed in PBS, and finally the fluorescence emission spectra of these dispersions were measured at excitation of 380 nm, respectively.

Drug loading for FRET-CMS

20 mL of Znq-CMS-SS-NH$_2$ aqueous dispersion (5 mg/mL) washed with appropriate amount of DMSO was dispersed in 20 mL of DMSO. 10 mL of 6-MP in DMSO (1 mg/mL) was added to the dispersion, and further stirred at room temperature for 12 h. The reacted solution was centrifuged, washed with DMSO to remove the free 6-MP, and redispersed in 20 mL of water, followed by adding slowly the already activated 30 mL of RhB-EA-HA solution (1 mg/mL) under stirring at room temperature for 24 h in the dark. FRET-CMS loaded with 6-MP (6-MP@FRET-CMS) were obtained by centrifugation at 10,000 rpm for 10 min and washed with water. The free 6-MP was determined by UV at 333 nm. The loading capacity and encapsulation efficiency were calculated by the following formulas: Loading efficiency = (weight of loaded drug)/(total weight of nanocarrier and drug) × 100%, and encapsulation efficiency = (weight of loaded drug)/(weight of initially added drug) × 100%.

Drug release study in vitro

6-MP@FRET-CMS nanoparticles (2 mg) were dispersed in 2 mL of corresponding buffer solution, which was sealed in a dialysis bag (cut off M_w = 14 Ka). The dialysis bag was soaked in 10 mL of 0.1 M of PBS corresponding solution (pH 5.0, 6.5, or 7.4) and placed in shaker at 37 ℃ with a shaking rate of 200 rpm, respectively. For the drug release, the different concentrations of glutathione (0 mM, 0.01 mM, 2 mM, 10 mM) were designed in this system. At predetermined time intervals, 1 mL of the sample solutions were withdrawn for analysis, and equivalent fresh corresponding buffer solutions were supplemented. The calibration curve of 6-MP was determined by the absorbance values of different concentrations of 6-MP at 333 nm. The amount of released 6-MP was based on a calibration curve with a series of diluted pure 6-MP solutions. The calibration curve fits the Lambert and Beers law well: $A = 0.0935C + 0.005$ ($R^2 = 0.999$), where A is the absorbance and C is the concentration of the sample (mg/mL).

BSA adsorption measurements

BSA adsorption measurements were investigated according to the reported method [38]. 60 mg bovine serum albumin (BSA) was completely dissolved in 100 ml of distilled water. 5 mg of CMS-SH, Znq-CMS, Znq-CMS-SS-NH$_2$, and FRET-CMS were dispersed in 5 ml of PBS solution, respectively, followed by the addition of 5 ml of BSA solution. Meanwhile, the control group was the mixture of 5 mL PBS and 5 mL BSA solution. The mixed solutions were shaken on a shaker for 4 h (150 rpm, 37 ℃). Subsequently, the mixtures were centrifuged, and then the supernatant of the solutions were collected. The concentrations of the residual BSA were determined by staining with Coomassie Brilliant Blue solution. 1 mL of the supernatants diluted tenfold with water were mixed with 5 mL of Coomassie Brilliant Blue solution to measure the absorbances of residual BSA using an automated microplate spectrophotometer at 595 nm. The amount of BSA adsorbed can be calculated using the following formula [1].

$$q = (C_i - C_f) \times 10 \times V/m \tag{1}$$

where C_i and C_f are the concentration of BSA in a control group and the residual BSA after adsorption, respectively; V is the total volume of the solution and m is the weight of the nanoparticles added to the solution.

Hemolysis assay

The hemolysis assay was carried out according to the previous report [45]. Rabbit blood cells (RBCs) were collected from 6 mL of rabbit whole blood by centrifugation at 1000 r/min for 10 min and washed five times with saline. 2 mL of washed RBCs was diluted with saline to a concentration of 2% (v: v). Then 2 mL of the diluted RBCs solution was mixed 2 mL of CMS-SH, Znq-CMS, Znq-CMS-SS-NH$_2$, and FRET-CMS dispersions at the different concentrations ranging from 20 to 1500 μg/mL, respectively, and then kept static for 4 h. The mixtures were

centrifuged at 1000 rpm for 10 min, and the absorbances of the supernatant were measured on a microplate reader at 541 nm. The hemolysis of RBCs in distilled water and saline was used as the positive and negative control, respectively. The hemolysis percentage was calculated through equation: Hemolysis percentages (%) = (absorbances of the sample – absorbances of negative control)/(absorbances of the positivecontrol-absorbances of negative control) × 100% [1].

Cell lines and culture

Both Hela and MCF-7 cells were cultured in DMEM culture medium supplemented with 10% (v/v) fetal bovine serum, 1% streptomycin–penicillin in a humidified atmosphere containing 5% CO_2 at 37 °C. The medium was routinely changed every 2 days and the cells were separated by trypsinization before reaching confluency.

Cytotoxicity assay in vitro

The cytotoxicity of 6-MP, Znq-CMS-SS-NH$_2$, blank, and 6-MP loaded of FRET-CMS was investigated with the standard MTT assay. Typically, HeLa and MCF-7 cells were incubated in a 96-well plate at a density of 10^4 cells/mL with 100 μL of culture medium per well. After full adhesion of cells, the medium was replaced with 100 μL of fresh medium containing different concentrations of the samples (serial concentrations of the 6-MP ranged from 0.01 to 30.0 μg/mL and the concentrations of the blank nanocarriers were equivalent to those in 6-MP-loaded nanoparticles). After being cocultured for 48 h, 20 μL of MTT PBS (5 mg/mL) was added into each well and incubation was carried out for another 4 h, the medium was removed and the formazan crystals formed by the living cells was dissolved in 150 μL of DMSO per well. The absorption of solution in per well was measured on a microplate reader at 490 nm. Cells without any treatment served as a normal control. Live/dead staining method was carried out to make the viable cells visualized. HeLa and MCF-7 cells were seeded in a 96-well plate at a density of $1 × 10^4$ per well and incubated with the samples with various concentrations for 48 h, the medium was removed and the cells were washed with PBS for three times. Each well was filled with 100 μL of staining reagent containing fluorescein diacetate (FDA, 6 mM) and propidium iodide (PI, 4 mM) for 10 min, washed twice with PBS, then added with 120 μL of PBS buffer and photographed under a fluorescence microscope. Viable cells were stained green, while dead cells were stained red.

Cellular uptake in vitro

Fluorescence microscope was used to investigate the targeted intracellular uptake of HA-Rhb (5 μg/mL), Znq-CMS,

FRET-CMS, and 6-MP@FRET-CMS (25 μg/mL) (containing with 6-MP concentration of 2.5 μg/mL). Hela and MCF-7 cells were incubated in a 24-well plate at a density of 105 cells/mL with a volume of 1 mL per well for full adhesion. Next, the medium was replaced with fresh medium containing the samples (6-MP concentration of 2.5 μg/mL) and incubated for different times (1 h, 2 h, or 4 h). The cells were then slightly rinsed with PBS three times to remove residual materials and fixed with 4% paraformaldehyde for 15 min, followed by the counterstaining with DAPI (100 ng/mL in PBS) for 10 min and washing with PBS twice. The fluorescent and phase contrast images of the cells were captured on the Olympus IX73 fluorescence inverted microscope with different channels and focus.

Characterization and statistical analysis

The TEM images were obtained on the JEOL JEM-2100F instrument and the FESEM images on S-4800 instrument. The DLS size and zeta potential of the nanoparticles were investigated by Malvern Zetasizer Nano ZS90. The isotherms of N_2 adsorption/desorption were obtained at 77 K using an ASAP 2020 accelerated surface area and porosity analyzer (Micromeritics, USA). The specific surface areas and the pore characteristics were estimated by Brunauer–Emmett–Teller (BET) and Barrett–Joyner–Halenda (BJH). ^{1}H NMR measurements were conducted in CDCl$_3$ using a Bruker AM-400 NMR spectrometer. Fourier transform infrared (FT-IR) spectra were noted on Nicolet 6700 FTIR spectrometer. UV–Vis absorption spectra were recorded on a PerkinElmer Lambda 35 spectrophotometer. Fluorescence emission spectra were measured on a PerkinElmer LS-55 fluorescence spectrophotometry. Fluorescence images were acquired with Olympus IX73 fluorescence inverted microscope. MTT assay was recorded at 490 nm using a Biotek Epoch Flash multifunctional microplate reader. The experimental data have been expressed as mean ± standard deviation (SD). The statistical analysis of variance (DAS ver1.0, Math Committee, Pharmacological Academy, China) was performed for comparison between the groups. $P < 0.05$ was considered as statistical level of significance.

Declarations

Conflict of interest The authors declare that they have no conflict of interest.

References

1. Q.F. Zhao, H.J. Geng, Y. Wang, Y.K. Gao, J.H. Huang, Y. Wang, J.H. Zhang, S.L. Wang, Hyaluronic acid oligosaccharide modified redox-responsive mesoporous silica nanoparticles for targeted drug delivery. ACS Appl. Mater. Interface **6**, 20290–20299 (2014)

2. H. Kim, S. Kim, C. Park, H. Lee, H.J. Park, C. Kim, Glutathione-induced intracellular release of guests from mesoporous silica nanocontainers with cyclodextrin gatekeepers. Adv. Mater. **22**, 4280–4283 (2010)

3. Y. Chen, W.P. Lu, Y.C. Guo, Y. Zhu, Y.P. Song, Chitosan-gated fluorescent mesoporous silica nanocarriers for the real-time monitoring of drug release. Langmuir **36**, 6749–6756 (2020)

4. J.M. Li, C.W.T. Leung, D.S.H. Wong, J.B. Xu, R. Li, Y.Y. Zhao, C.Y.Y. Yung, E.G. Zhao, B.Z. Tang, L.M. Bian, Photocontrolled SiRNA delivery and biomarker-triggered luminogens of aggregation-induced emission by up-conversion NaYF4:Yb3+Tm3+@ SiO2 nanoparticles for inducing and monitoring stem-cell differentiation. ACS Appl. Mater. Interfaces **11**, 22074–22084 (2019)

5. Z. Li, J.C. Barnes, A. Bosoy, J.F. Stoddart, J.I. Zink, Mesoporous silica nanoparticles in biomedical applications. Chem. Soc. Rev. **41**, 2590–2605 (2012)

6. X.Y. Zhang, X.Q. Zhang, S.Q. Wang, M.Y. Liu, Y. Zhang, L. Tao, Y. Wei, Facile incorporation of aggregation-induced emission materials into mesoporous silica nanoparticles for intracellular imaging and cancer therapy. ACS Appl. Mater. Interface **5**, 1943–1947 (2013)

7. M. Liong, J. Lu, M. Kovochich, T. Xia, S.G. Ruehm, A.E. Nel, F. Tamanoi, J.I. Zink, Multifunctional inorganic nanoparticles for imaging, targeting, and drug delivery. ACS Nano **2**, 889–896 (2008)

8. J.E. Lee, N. Lee, T. Kim, J. Kim, T. Hyeon, Multifunctional mesoporous silica nanocomposite nanoparticles for theranostic applications. Acc. Chem. Res. **44**, 893–902 (2011)

9. P. Singh, S. Srivastava, S.K. Singh, Nanosilica: recent progress in synthesis, functionalization, biocompatibility, and biomedical applications. ACS Biomater. Sci. Eng. **5**, 4882–4898 (2019)

10. S. Jafari, H. Derakhshankhah, L. Alaei, A. Fattahi, B.S. Varnamkhasti, A.A. Saboury, Mesoporous silica nanoparticles for therapeutic/diagnostic applications. Biomed. Pharmacother. **109**, 1100–1111 (2019)

11. Y. Zhang, Q. Yue, M.M. Zagho, J.J. Zhang, A.A. Elzatahry, Y.J. Jiang, Y.H. Deng, Core-shell magnetic mesoporous silica microspheres with large mesopores for enzyme immobilization in biocatalysis. ACS Appl. Mater. Interface **11**, 10356–10363 (2019)

12. T. Zhang, B.T. Huang, A.A. Elzatahry, A. Alghamdi, Q. Yue, Y.H. Deng, Synthesis of podlike magnetic mesoporous silica nanochains for use as enzyme support and nanostirrer in biocatalysis. ACS Appl. Mater. Interface **12**, 17913–17920 (2020)

13. A.J. Salinas, P. Esbrit, M. Vallet-Regi, A tissue engineering approach based on the use of bioceramics for bone repair. Biomater Sci-Uk. **1**, 40–51 (2013)

14. N. Ehlert, P.P. Mueller, M. Stieve, T. Lenarz, P.J.C.S.R. Behrens, Nanoporous silica films as novel biomaterial: applications in the middle ear. Chem. Soc. Rev. **42**, 3847–3861 (2013)

15. P.P. Yang, S.L. Gai, J. Lin, Functionalized mesoporous silica materials for controlled drug delivery. Chem. Soc. Rev. **41**, 3679–3698 (2012)

16. A. Schlossbauer, J. Kecht, T.J.A.C.I.E. Bein, Biotin-Avidin as a protease-responsive cap system for controlled guest release from colloidal mesoporous silica. Angew. Chem. **121**, 3138–3141 (2009)

17. S. Giri, B.G. Trewyn, M.P. Stellmaker, V.S. Lin, Stimuli-responsive controlled-release delivery system based on mesoporous silica nanorods capped with magnetic nanoparticles. Angew. Chem. **44**, 5038–5044 (2005)

18. Z.Z. Shi, C.B. Yang, R. Li, L.P. Ruan, Microwave thermal-triggered drug delivery using thermosensitive peptide-coated core-shell mesoporous silica nanoparticles. J. Mater. Sci. **55**, 6118–6129 (2020)

19. A. Schlossbauer, S. Warncke, P.M.E. Gramlich, J. Kecht, A. Manetto, T. Carell, T. Bein, A programmable DNA-based molecular valve for colloidal mesoporous silica. Angew. Chem. Int. Edit. **49**, 4734–4737 (2010)

20. L.P. Ruan, W. Chen, R.N. Wang, J. Lu, J.I. Zink, Magnetically stimulated drug release using nanoparticles capped by self-assembling peptides. Acs Appl Mater Interface **11**, 43835–43842 (2019)

21. R. Han, S. Wu, K. Tang, Y. Hou, Facilitating drug release in mesoporous silica coated upconversion nanoparticles by photoacid assistance upon near-infrared irradiation. Adv. Powder Technol. **31**, 3860–3866 (2020)

22. D.P. Ferris, Y.L. Zhao, N.M. Khashab, H.A. Khatib, J.F. Stoddart, J.I. Zink, Light-operated mechanized nanoparticles. J Am Chem Soc. **131**, 1686–1688 (2009)

23. W. Cheng, J.P. Nie, L. Xu, C.Y. Liang, Y. Peng, G. Liu, T. Wang, L. Mei, L.Q. Huang, X.W. Zeng, pH-sensitive delivery vehicle based on folic acid-conjugated polydopamine-modified mesoporous silica nanoparticles for targeted cancer therapy. Acs Appl. Mater. Interface **9**, 18462–18473 (2017)

24. T.T.H. Thi, V.D. Cao, T.N.Q. Nguyen, D.T. Hoang, V.C. Ngo, D.H. Nguyen, Functionalized mesoporous silica nanoparticles and biomedical applications. Mater. Sci. Eng. C **99**, 631–656 (2019)

25. J.J. Liu, B.L. Zhang, Z. Luo, X.W. Ding, J.H. Li, L.L. Dai, J. Zhou, X.J. Zhao, J.Y. Ye, K.Y. Cai, Enzyme responsive mesoporous silica

nanoparticles for targeted tumor therapy in vitro and in vivo. Nanoscale **7**, 3614–3626 (2015)

26. A. Schlossbauer, J. Kecht, T. Bein, Biotin-avidin as a protease-responsive cap system for controlled guest release from colloidal mesoporous silica. Chem. Int. Edit. **48**, 3092–3095 (2009)

27. A. Jana, K.S.P. Devi, T.K. Maiti, N.D.P. Singh, Perylene-3-ylmethanol: fluorescent organic nanoparticles as a single-component photoresponsive nanocarrier with real-time monitoring of anticancer drug release. J. Am. Chem. Soc. **134**, 7656–7659 (2012)

28. M.H. Lee, J.Y. Kim, J.H. Han, S. Bhuniya, J.L. Sessler, C. Kang, J.S. Kim, Direct fluorescence monitoring of the delivery and cellular uptake of a cancer-targeted RGD peptide-appended naphthalimide theragnostic prodrug. J. Am. Chem. Soc. **134**, 12668–12674 (2012)

29. K. Ock, W.I. Jeon, E.O. Ganbold, M. Kim, J. Park, J.H. Seo, K. Cho, S.W. Joo, S.Y. Lee, Real-time monitoring of glutathione-triggered thiopurine anticancer drug release in live cells investigated by surface-enhanced Raman scattering. Anal. Chem. **84**, 2172–2178 (2012)

30. S. Santra, C. Kaittanis, O.J. Santiesteban, J.M. Perez, Cell-specific, activatable, and theranostic prodrug for dual-targeted cancer imaging and therapy. J. Am. Chem. Soc. **133**, 16680–16688 (2011)

31. H. Li, Y.Q. Fu, L.B. Zhang, X.M. Liu, Y. Qu, S.T. Xu, C.L. Lu, In situ route to novel fluorescent mesoporous silica nanoparticles with 8-hydroxyquinolinate zinc complexes and their biomedical applications. Micropor. Mesopor. Mater. **151**, 293–302 (2012)

32. J.P. Cross, P.G. Sammes, A useful 8-hydroxyquinoline synthon. ChemInform **35**, 703–705 (2004)

33. B.P. Toole, Hyaluronan: from extracellular glue to pericellular cue. Nat. Rev. Cancer **4**, 528–539 (2004)

34. C. Surace, S. Arpicco, A. Dufay-Wojcicki, V. Marsaud, C. Bouclier, D. Clay, L. Cattel, J.M. Renoir, E. Fattal, Lipoplexes targeting the CD44 hyaluronic acid receptor for efficient transfection of breast cancer cells. Mol. Pharm. **6**, 1062–1073 (2009)

35. W. Wanxia, W. Youyun, W. Yu, G. Huameng, Z. Hongda, L. Mingxing, Redox/pH dual stimuli-responsive ZnO QDs-gated mesoporous silica nanoparticles as carriers in cancer therapy. IET Nanobiotechnol. **13**, 640–649 (2019)

36. M.J. Vold, in *Zeta Potential in Colloid Science. Principles and Applications*, ed. R. J. Hunter, (Academic Press, New York, 1982), p. 608

37. R. Cheng, F.H. Meng, C. Deng, H.A. Klok, Z.Y. Zhong, Dual and multi-stimuli responsive polymeric nanoparticles for programmed site-specific drug delivery. Biomaterials **34**, 3647–3657 (2013)

38. T. Arnebrant, M. Wahlgren, Protein—surfactant interactions at solid surfaces. Adv. Colloid Interface Sci. **57**, 239–254 (1995)

39. T. Nash, A.C. Allison, J.S. Harington, Physico-chemical properties of silica in relation to its toxicity. Nature **210**, 259–261 (1966)

40. I.I. Slowing, C.W. Wu, J.L. Vivero-Escoto, V.S. Lin, Mesoporous silica nanoparticles for reducing hemolytic activity towards mammalian red blood cells. Small **5**, 57–62 (2009)

41. M. Diociaiuti, F. Bordi, L. Gataleta, G. Baldo, P. Crateri, L. Paoletti, Morphological and functional alterations of human erythrocytes induced by SiO2 particles: an electron microscopy and dielectric spectroscopy study. Environ. Res. **80**, 197–207 (1999)

42. C.X. Yang, M.L. Cao, H. Liu, Y.Q. He, J. Xu, Y. Du, Y.W. Liu, W.J. Wang, L. Cui, J.J. Hu, F. Gao, The high and low molecular weight forms of hyaluronan have distinct effects on CD44 clustering. J. Biol. Chem. **287**, 43094–43107 (2012)

43. C.X. Yang, Y.W. Liu, Y.Q. He, Y. Du, W.J. Wang, X.X. Shi, F. Gao, The use of HA oligosaccharide-loaded nanoparticles to breach the endogenous hyaluronan glycocalyx for breast cancer therapy. Biomaterials **34**, 6829–6838 (2013)

44. H.M. Gong, Z.F. Xie, M.X. Liu, H.D. Zhu, H.H. Sun, Redox-sensitive mesoporous silica nanoparticles functionalized with PEG through a disulfide bond linker for potential anticancer drug delivery. Rsc Adv. **5**, 59576–59582 (2015)

45. L. Chen, W. Feng, X.J. Zhou, K.X. Qiu, Y.K. Miao, Q.Q. Zhang, M. Qin, L. Li, Y.Z. Zhang, C.L. He, Facile synthesis of novel albumin-functionalized flower-like MoS2 nanoparticles for in vitro chemo-photothermal synergistic therapy. Rsc Adv. **6**, 13040–13049 (2016)